

# Planet cartography with neural learned regularization

A. Asensio Ramos and E. Pallé

<sup>1</sup> Instituto de Astrofísica de Canarias (IAC), Avda Vía Láctea S/N, 38200 La Laguna, Tenerife, Spain  
e-mail: andres.asensio@iac.es

<sup>2</sup> Departamento de Astrofísica, Universidad de La Laguna, 38205 La Laguna, Tenerife, Spain

Received ; accepted

## ABSTRACT

**Aims.** Finding potential life harboring exo-Earths is one of the aims of exoplanetary science with the use of future telescopes. Detecting signatures of life in exoplanets will likely first be accomplished by determining the bulk composition of the planetary atmosphere via reflected/transmitted spectroscopy. However, a complete understanding of the habitability conditions will surely require mapping the presence of liquid water, continents and/or clouds. Spin-orbit tomography is a technique that allows us to obtain maps of the surface of exoplanets around other stars using the light scattered by the planetary surface.

**Methods.** We leverage the enormous potential of deep learning and propose a mapping technique for exo-Earths in which the regularization is learned from mock surfaces. The solution of the inverse mapping problem is posed as a deep neural network that can be trained end-to-end with suitable training data. Since we still lack observational data of the surface albedo of exoplanets, we propose in this work to use methods based on the procedural generation of planets, inspired by what we found on Earth. We also consider mapping the recovery of surfaces and the presence of persistent cloud in cloudy planets, a much more challenging problem.

**Results.** We show that a reliable mapping can be carried out with our approach, producing very compact continents, even when using single passband observations. More importantly, if exoplanets are partially cloudy like the Earth is, we show that one can potentially map the distribution of persistent clouds that always occur on the same position on the surface (associated to orography and sea surface temperatures) together with non-persistent clouds that move across the surface. This will become the first test one can perform on an exoplanet for the detection of an active climate system. For small rocky planets in the habitable zone of their stars, this weather system will be driven by water, and the detection can be considered as a strong proxy for truly habitable conditions.

**Key words.** methods: numerical — planets and satellites: surfaces, terrestrial planets

## 1. Introduction

One of the most promising goals in the field of exoplanets is to reach the technical capability to characterize the bulk composition of rocky exoplanet atmospheres. In particular, for those small planets within the habitable zone of their host star, which will in turn open the search for the combination of gaseous species that could be classified as a biomarker (Des Marais et al. 2002). With more than 4000 planets detected to date, the number of small rocky planets is also large, and it continues to increase thanks to space missions like Kepler and TESS as well as ground-based photometric and radial velocity surveys. The majority of this small rocky planets, however, transit around M-type stellar hosts (Hardegree-Ullman et al. 2019). This is good news as these small stars offer a greater chance for planetary characterization owing to a reduced star/planet contrast ratio. In the coming future, ultra-stable high resolution spectrographs, such as ESPRESSO, mounted on large aperture telescopes (ELTs) will allow the detection of small rocky planets around K and G type stars.

The initial characterization of small rocky planets will probably be allowed by transmission spectroscopy of targets around M-type stars (Pallé et al. 2011; Snellen et al. 2013), although whether those planets can sustain an atmosphere is still open to debate, and more so the possibility of these planets to host life (Tarter et al. 2007; Luger & Barnes 2015). On the longer term, direct imaging of habitable zone exoplanets will be accom-

plished by space-base coronagraphic or interferometric techniques (Léger et al. 1996). This expansion into reflected light studies is crucial for our understanding of planetary atmospheres (and possible biomarkers) in the solar neighborhood, as for an Earth-Sun twin the transit probability is only 0.5%, meaning that only one of the closest 200 earths-like planets will transit its host star.

Characterizing planets via reflected light poses a technical challenge, but it also offers the possibility of a more in-depth characterization. For example, we will be sensitive to light reflected from the surface, and measure the bulk composition of the full atmosphere, as opposed to transmission spectroscopy where only the higher levels of the atmosphere are probed (Pallé et al. 2009). The initial characterization of a planetary atmospheres with reflected light will surely come from single-epoch spectroscopy, which will allow the detection of the bulk composition of the atmosphere, searching for species such as H<sub>2</sub>O, CO<sub>2</sub>, or O<sub>2</sub>, which might be enough to classify the planet as inhabitable/inhabited (Meadows et al. 2018). However, the temporal variability information introduced by cloud-tops and surface reflectance is very rich and can provide crucial additional details on the existence of continental land masses from single or multi-color photometry (Ford et al. 2001). When clouds come into the picture, retrieving a surface map is not so straightforward, but with enough data it can provide insights into the existence of a dynamic weather system (Pallé et al. 2008).

Mapping the surface of exoplanets around other stars using the light scattered by the planetary surface was proposed by Kawahara & Fujii (2010). Under some approximations, the light scattered by the planet can be linearly related to the albedo properties of the surface. Mapping the surface albedo by solving the inverse problem turns out to be, like many other linear and non-linear problems, ill-posed. There is not enough information on the light curve to fully constrain the solution and some kind of regularization has to be used. Kawahara & Fujii (2011) formulated the inverse problem, named spin-orbit tomography (SOT) and proposed a solution based on the Tikhonov regularization. The general idea is that if one observes a spinning planet orbiting around a star for a sufficiently long time and with enough time cadence, one can reconstruct the surface albedo from the time modulation of the light curve. This was indeed nicely demonstrated by Fujii & Kawahara (2012), who showed that approximate albedo maps can be obtained for planets with different orbital configurations.

After the initial idea of SOT, other approaches to the solution of the inverse problem have been suggested. Farr et al. (2018) proposed to use a Gaussian Process (GP) as a prior for the surface albedo map in the pixel domain and deal with the inversion in the Bayesian framework. This allowed Farr et al. (2018) to produce 2D mappings with uncertainties and show that a planet can be mapped with a very limited amount of observations. This work has been recently extended by Kawahara & Masuda (2020) to also propose a GP in time as a prior of the time evolution of the surface. This can be used for planets with moving surfaces or with clouds that evolve in time. Luger et al. (2019a) developed *starry*, a computer code which uses spherical harmonics as a basis set of the albedo surface of a planet. Apart from a very compact representation of the surface albedo, this representation also leads to an efficient acceleration of the computations. This allowed Luger et al. (2019b) to map a mock Earth using synthetic TESS data. Berdyugina & Kuhn (2019) later proposed an Occamian approach for the solution of the inverse problem, which is essentially equivalent to solving the linear inverse problem using the singular value decomposition (SVD). Recently, Aizawa et al. (2020) leveraged the recent theories of compressed sensing and sparse reconstruction (Candès et al. 2006) to show that such sparse reconstructions (also discussed in the next section) lead to an improved mapping of the surface, with better constrained continents. More recently, Kawahara (2020) used non-negative matrix factorization to show how to map exoplanets using different colors.

All previous approaches are based on some form of mathematical regularization. While Tikhonov regularization tends to generate smooth maps, sparse regularization produces a better mapping with more defined continents. GP priors (both spatial and temporal) open up the possibility of using Bayesian inference but sometimes produce overly smooth results. In this paper we leverage the enormous potential of deep learning (Goodfellow et al. 2016) and propose a mapping technique for exo-Earths in which the regularization is learned from simulations. The solution of the inverse mapping problem is posed as a deep neural network that can be trained end-to-end with suitable training data. Since we still lack observational data of the surface albedo of exoplanets, our results depend on our ability to generate mock surfaces. We propose in this work to use methods based on the procedural generation of planets that are inspired by the appearance of the Earth’s real surface and clouds properties.

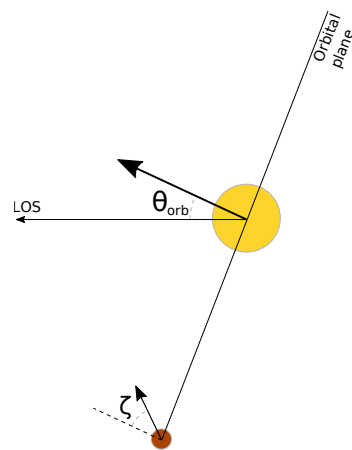


**Fig. 1.** Schematic illustration of the orbital configuration. The orbital plane is defined by the angle  $\theta_{\text{orb}}$ , while the planet spins forming an obliquity angle  $\zeta$  with respect to the orbital plane normal.

## 2. Mapping cloudless planets

### 2.1. Formulation of the problem

The ratio between the light scattered by the surface of an exoplanet orbiting around a certain star and the incoming flux of the star is, in general, a complex function of the geometry of scattering and the properties of the scatterers. In the single scattering approximation and assuming scattering is isotropic (Lambertian), this function only depends on geometry.

For a given time  $t_i$ , the integrated stellar light reflected from an exoplanet is given by the following linear relation when the planetary surface is conveniently discretized:

$$d_i = \sum_j \Phi_{ij} m_j, \quad (1)$$

where  $d_i$  is the relative flux observed at time  $t_i$  and  $m_j$  is the  $j$ -th surface element albedo of the discretized planetary surface. The matrix elements  $\Phi_{ij}$  are purely geometrical, and depend on the relative position of the  $j$ -th surface element of the planet, the star and the observer at time  $t_i$ . In matrix form, and assuming a realistic observation, we have:

$$\mathbf{d} = \mathbf{\Phi} \mathbf{m} + \boldsymbol{\epsilon}, \quad (2)$$

where  $\boldsymbol{\epsilon}$  is Gaussian noise with zero mean and variance  $\sigma_n$ . The matrix  $\mathbf{\Phi}$ , also known as the geometric kernel, depends on the following set of parameters of the planet (see Fig. 1): the rotation period ( $P_{\text{rot}}$ ), the orbital period ( $P_{\text{orb}}$ ), the initial rotational and orbital phases ( $\phi_{\text{rot}}$  and  $\phi_{\text{orb}}$ , respectively), the orbit inclination  $\theta_{\text{orb}}$  and the obliquity of the planet  $\zeta$ .

When observations are available, it is possible to invert the previous linear relation. Given that the problem is ill-defined, the solution is often regularized, so that one needs to solve the following maximum a-posteriori problem:

$$\arg \min_m \frac{1}{2} \|\mathbf{d} - \mathbf{\Phi} \mathbf{m}\|_2^2 + \lambda R(\mathbf{m}), \quad (3)$$

where the log-likelihood (first term) is a direct consequence of the assumption of uncorrelated Gaussian noise, while  $R(\mathbf{m})$  plays the role of a convex log-prior that is used to regularize the result. Several different options have been used in the literature, as described in the Introduction. The first one is Tikhonov regularization, for which  $R(\mathbf{m}) = \|\mathbf{m} - \hat{\mathbf{m}}\|_2^2$ . This regularization pushes the

solution to  $\hat{\mathbf{m}}$  when no information is available. More recently, sparse regularization (or  $\ell_1$  regularization) has also been considered directly on the albedo surface, so that  $R(\mathbf{m}) = \|\mathbf{m}\|_1$ <sup>1</sup>. It is also interesting to point out that this regularization can also be applied in a transformed domain with  $R(\mathbf{m}) = \|\mathbf{W}\mathbf{m}\|_1$ , where  $\mathbf{W}$  is often a linear orthonormal transformation with a fast transform operator, like Fourier or wavelet. Aizawa et al. (2020) assumed sparsity on the pixel space (large regions of the planet have small albedos compatible with zero), but it might well be that the solution is ever sparser in a transformed domain.

## 2.2. Deep neural network regularized reconstruction with loop unrolling

A conceptually simple, often fast, and successful method for the solution of convex regularized problems is the iterative shrinkage thresholding algorithm (ISTA; Beck & Teboulle 2009). ISTA is a first order proximal algorithm (Parikh & Boyd 2013) for the optimization of the following type of problems:

$$\arg \min_{\mathbf{x}} f(\mathbf{x}) + g(\mathbf{x}), \quad (4)$$

where  $f(\mathbf{x})$  is differentiable and  $g(\mathbf{x})$  is a convex function. The solution is obtained by the iterative application of the following steps:

$$\mathbf{r}^{(k)} = \mathbf{x}^{(k-1)} - \rho \nabla f(\mathbf{x}) \quad (5)$$

$$\mathbf{x}^{(k)} = \text{prox}_g(\mathbf{r}^{(k)}) = \arg \min_{\mathbf{y}} \frac{1}{2} \|\mathbf{y} - \mathbf{r}^{(k)}\|_2^2 + g(\mathbf{y}), \quad (6)$$

where  $\rho$  is a step size that needs to be properly tuned. The ISTA algorithm (and fundamentally all algorithms for the solution of regularized problems) crucially depend on the availability of a fast way to solve subproblem (6), which is known as the proximal operator. Fortunately, it is possible to find a closed form for the proximal operator for certain  $g(\mathbf{x})$  functions. Of special interest are the case of  $\ell_1$  and Tikhonov regularizations. The proximal operator for the  $\ell_1$  regularization, where  $g(\mathbf{x}) = \|\mathbf{W}\mathbf{x}\|_1$ , is given by:

$$\text{prox}_{\|\mathbf{W}\cdot\|_1}(\mathbf{x}) = \mathbf{W}^T \text{soft}(\mathbf{W}\mathbf{x}, \lambda), \quad (7)$$

where the soft thresholding (or shrinkage) operator is given by:

$$\text{soft}(x, \lambda) = \max(x - \lambda, 0) \frac{x}{|x|}. \quad (8)$$

The proximal operator for the Tikhonov regularization, in which  $g(\mathbf{x}) = \|\mathbf{x}\|_2$ , is given by

$$\text{prox}_{\|\cdot\|_2}(\mathbf{x}) = \max\left(1 - \frac{\lambda}{\|\mathbf{x}\|_2}, 0\right) \mathbf{x}. \quad (9)$$

Particularizing the ISTA method to Eq. (3), the iterative scheme is given by:

$$\mathbf{r}^{(k)} = \mathbf{m}^{(k-1)} - \rho \Phi^T (\Phi \mathbf{m}^{(k-1)} - \mathbf{d}) \quad (10)$$

$$\mathbf{m}^{(k)} = \text{prox}_{\lambda R}(\mathbf{r}^{(k)}) = \arg \min_{\mathbf{x}} \frac{1}{2} \|\mathbf{x} - \mathbf{r}^{(k)}\|_2^2 + \lambda R(\mathbf{x}), \quad (11)$$

where the step size  $\rho$  has an optimal value given by  $\rho \leq (2\tau)^{-1}$ , where  $\tau$  is the largest eigenvalue of the  $\Phi^T \Phi$  matrix.

We propose to solve the regularized problem by leveraging deep neural networks to impose the regularization. Instead of

explicitly defining the regularization function  $R(\mathbf{m})$ , we directly model its effect as a proximal projection with the aid of a neural network, so we substitute Eq. (11) by:

$$\mathbf{m}^{(k)} = \text{prox}_{\lambda R}(\mathbf{r}^{(k)}) = F^{(k)}(\mathbf{r}^{(k)}), \quad (12)$$

where the  $F^{(k)}(\mathbf{x})$  are mappings defined by convolutional neural networks whose architecture we discuss below. The  $F^{(k)}(\mathbf{x})$  operators can then be seen as *learned denoisers* that generalize the concept of a proximal projection operator (e.g., Venkatakrishnan et al. 2013; Zhang & Ghanem 2018; Wang et al. 2019). Such iterative methods are commonly known as *plug-and-play methods*.

We follow Gregor & LeCun (2010) and unroll  $N$  iterations of Eqs. (10) and (12) as a deep neural network and train the network end-to-end. The loop unrolling also allows us to learn optimal values for  $\rho$  used in the ISTA iteration. We also allow them to be different at all iterations, not like ISTA in which they are kept constant. For clarity, we repeat here the two steps that need to be iterated for  $k = 1, \dots, N$ , starting from an initial solution  $\mathbf{m}^{(0)} = \mathbf{0}$ :

$$\mathbf{r}^{(k)} = \mathbf{m}^{(k-1)} - \rho \rho^{(k)} \Phi^T (\Phi \mathbf{m}^{(k-1)} - \mathbf{d}) \quad (13)$$

$$\mathbf{m}^{(k)} = F^{(k)}(\mathbf{r}^{(k)}). \quad (14)$$

The learned quantities are forced to fulfill  $\rho^{(k)} \sim 1$  and are used to allow our trained unrolled scheme to use step sizes different than the optimal one given by  $\rho$ . We have found that the chosen initial solution gives stable reconstructions, although one can also use other potentially interesting options like  $\mathbf{m}^{(0)} = \Phi^T \mathbf{d}$ .

The general structure of the unrolled deep network is displayed in Fig. 2. The inputs to the network are the vector of observations  $\mathbf{d}$  and the initial solution  $\mathbf{m}^{(0)}$ . These vectors are then used to compute  $\mathbf{r}^{(k)}$ , which is then transformed by the non-linear neural network to finally produce a new estimated solution. This process is iterated  $N$  times. The detail of the neural networks is shown as an inset in Fig. 2. The specifics of these networks is discussed in the following.

## 2.3. Denoisers

Several options are available for the layers inside the  $F$  operators. The first obvious option is to use a fully connected layer to map the HEALPix pixelization, seen as a one-dimensional vector, to intermediate representations. We quickly discarded this option because the number of free parameters of the network increases very fast with the number of pixels in the sphere. The second option is to use convolutional layers, which are very efficient in the number of parameters. Our first option is what we term an *1D regularizer*, that uses convolutional layers acting on the HEALPix pixelization seen as a one-dimensional vector. This option does not exploit any specific spatial correlation in the surface of the exoplanet. As indicated in Fig. 2, we utilize four 1D convolutional layers with kernels of size 3 producing the sequence  $(1, N_s) \rightarrow (32, N_s) \rightarrow (32, N_s) \rightarrow (32, N_s) \rightarrow (1, N_s)$ , where the first index indicates the number of channels and the second index indicates the number of pixels on the surface. We unroll  $N = 15$  iterations, with a total number of  $\sim 95\text{k}$  free parameters. An arguably more appropriate option, that we term as an *2D regularizer*, is to use convolutional layers defined on the surface of the sphere using the HEALPix pixelization. We take advantage of the idea developed by Krachmalnicoff & Tomasi (2019). This option has the interesting property of exploiting the spatial information on the sphere to produce an intermediate representation. In this case we also use 32 kernels of size  $3 \times 3$  in the

<sup>1</sup> We note that the  $\ell_1$  norm of a vector is given by  $\|\mathbf{x}\|_1 = \sum_i |x_i|$ .

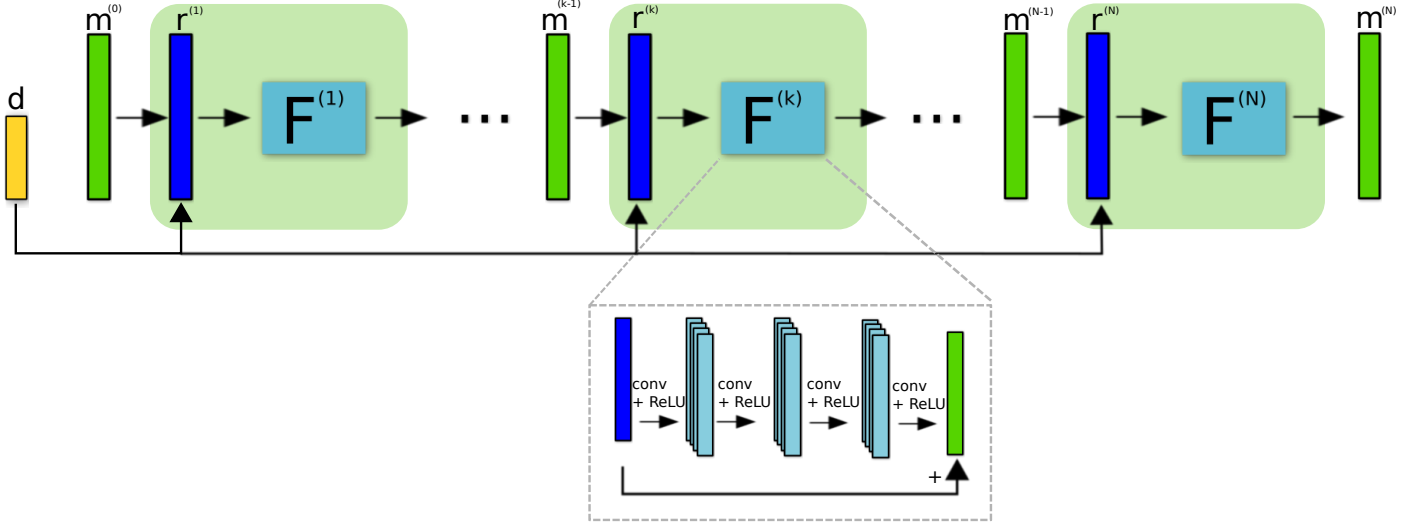


**Fig. 2.** Architecture of the deep neural network that carries out the unrolled iterative reconstruction for  $N$  steps. Each green phase plate defines the application of Eqs. (25) and (27). The internal structure of the  $F$  operator is shown in the inset. These operators are made of a train of convolutional layers with ReLU activation functions that generate  $N_f$  channels. The last layer, followed by a ReLU activation function and another linear layer.

intermediate layers, resulting in a total of 285k free parameters. We caution that the solution of Krachmalnicoff & Tomasi (2019) for implementing convolutions on the sphere is arguably not the most optimal, producing artifacts that we discuss in the following sections. It is worth exploring other options for convolutions in the sphere (e.g., Perraudin et al. 2019).

#### 2.4. Tikhonov regularization

For comparison with our results we consider the Tikhonov-regularized case. We solve it using ISTA with the corresponding proximal projection operator, given by Eq. (9):

$$\mathbf{r}^{(k)} = \mathbf{m}^{(k-1)} - \rho \Phi^T (\Phi \mathbf{m}^{(k-1)} - \mathbf{d}) \quad (15)$$

$$\mathbf{m}^{(k)} = \max \left( 1 - \frac{\lambda}{\|\mathbf{r}^{(k)}\|_2}, 0 \right) \mathbf{r}^{(k)}, \quad (16)$$

starting from  $\mathbf{m}^{(0)} = 0$ .

### 3. Mapping cloudy planets

Mapping cloudy planets is a much more challenging problem than mapping cloudless planets. If exoplanets are similar to the Earth, one can potentially find persistent clouds that always occur on the same position on the surface together with non-persistent clouds that form or move across the surface (e.g., Pallé et al. 2008). Persistent clouds can hardly be distinguished from the surface albedo, but non-persistent clouds make the recovery of the surface much more difficult. Our aim here is to show that this mapping can be carried out even when using single passband observations, although the mapping can potentially improve if multi-band observations are considered.

We consider two models for the resulting albedo in a planet with clouds. For the first one, let us assume, for a discretized element in the surface of the planet, that  $m_s$  is the surface albedo while  $m_c$  is the cloud albedo. We make the assumption that the clouds are kept stationary during a single epoch of observations to reduce the dimensionality of the solution space. We also make the assumption that clouds have a fairly low absorption in the visible while scattering is dominant. If the stellar illumination

arriving at the atmosphere of the planet is  $F_0$ , the amount of light reflected by the cloud would be  $F_0 m_c$ . A fraction  $F_0(1 - m_c)$  would pass downward and reflect off the planetary surface. The amount of reflected light would then be  $F_0(1 - m_c)m_s$ . On its return upward, a fraction  $m_c$  is again dispersed and a fraction  $(1 - m_c)$  would pass to the external layers of the atmosphere. Therefore, from this amount of light that comes out again once can infer the final albedo of the planet, which is  $m = m_c + m_s(1 - m_c)^2$ . By plugging this expression into Eq. (1) for all surface elements, one ends up with the following generative model for the observed flux at epoch  $i$  from a total of  $N_e$  epochs:

$$\mathbf{d}_i = \Phi_i (\mathbf{m}_{c,i} + \mathbf{m}_s \odot (1 - \mathbf{m}_{c,i})^2) + \epsilon, \quad (17)$$

where  $\odot$  is the Hadamard (or elementwise) product. We note that the problem is still linear in the albedo of the planetary surface if the cloud albedo is known. On the other contrary, the problem is already non-linear in the cloud albedo. We note that  $\mathbf{m}_s$  is common to all epochs and plays the role of  $\mathbf{m}$  in the cloudless planet. A direct application of Eqs. (5) and (6) results in the following iterative scheme:

$$\mathbf{r}_s^{(k)} = \mathbf{m}_s^{(k-1)} - 2\rho\rho^{(k)} \sum_{i=1}^{N_e} \mathbf{t}_{2,i} \odot \mathbf{t}_{1,i} \quad (18)$$

$$\mathbf{m}_{c,i}^{(k)} = \mathbf{m}_{c,i}^{(k-1)} - 2\rho\rho^{(k)} (\mathbf{t}_{2,i} - 2\mathbf{t}_{2,i} \odot \mathbf{m}_s^{(k-1)} \odot \mathbf{t}_{0,i}) \quad (19)$$

$$\mathbf{m}_s^{(k)} = F^{(k)}(\mathbf{r}_s^{(k)}). \quad (20)$$

where

$$\mathbf{t}_{0,i} = 1 - \mathbf{m}_{c,i}^{(k-1)} \quad (21)$$

$$\mathbf{t}_{1,i} = \mathbf{t}_{0,i} \odot \mathbf{t}_{0,i} \quad (22)$$

$$\mathbf{t}_{2,i} = \Phi_i^T [\Phi_i (\mathbf{m}_{c,i}^{(k-1)} + \mathbf{t}_{1,i} \odot \mathbf{m}_s^{(k-1)}) - \mathbf{d}]. \quad (23)$$

The  $F^{(k)}$  operators are trained by unrolling the previous iterative scheme  $N$  times and dealing with them as an end-to-end neural network, as before.

A second model, slightly less complex, can also be considered. In this model we assume that the intrinsic albedo of the clouds is fixed to a value  $A_c$ . The clouds are then characterized

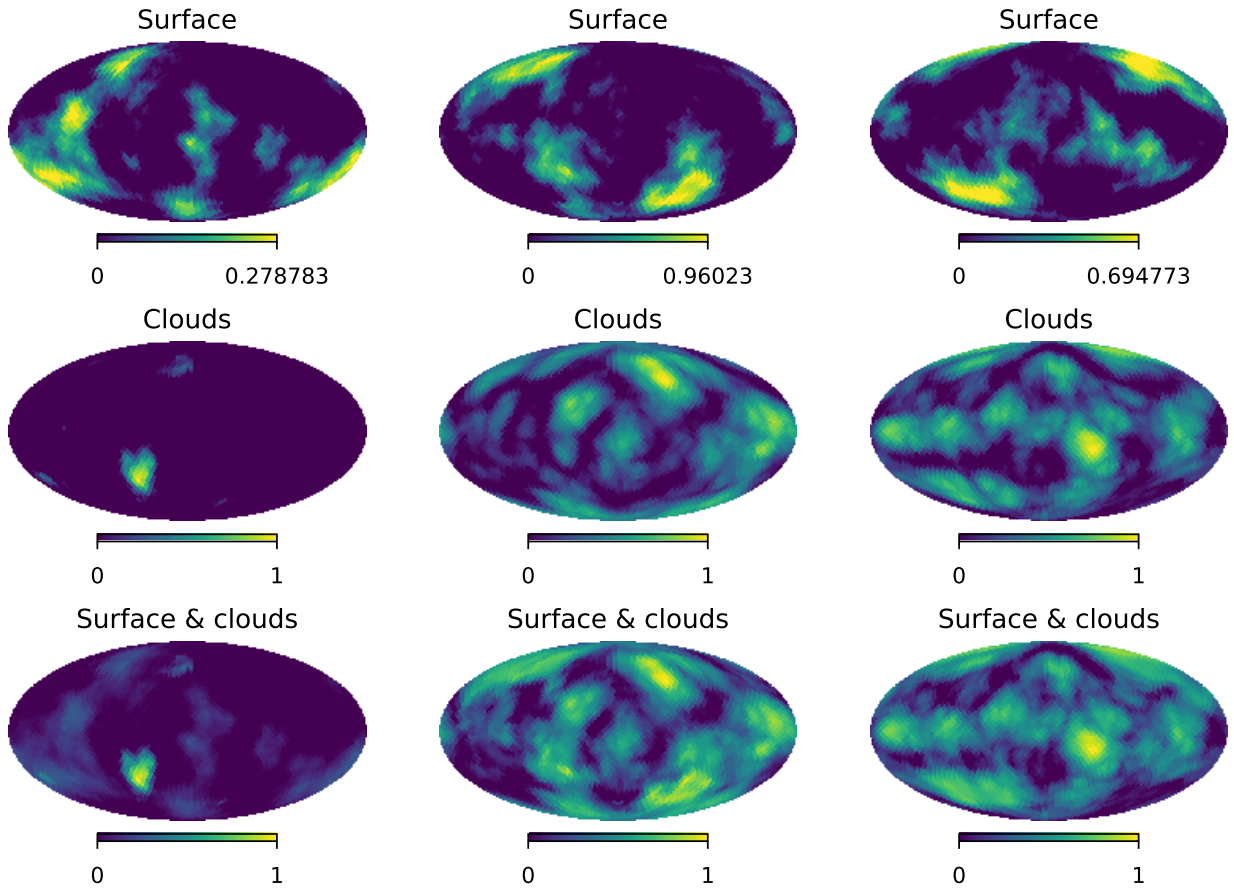


**Fig. 3.** Samples of mock planetary (upper row) and cloud (middle row) albedo surfaces that are part of the training set. The combination of the two is shown in the lower row.

by the coverage filling factor,  $\mathbf{m}_{c;i}$ , inside each discrete pixel on the surface of the planet at each epoch. Under this approximation, the observed light curve is given by:

$$\mathbf{d}_i = \Phi_i (\mathbf{m}_s + (A_c - \mathbf{m}_s) \odot \mathbf{m}_{c;i}) + \epsilon. \quad (24)$$

In this case, the iterative scheme is given by:

$$\mathbf{r}_s^{(k)} = \mathbf{m}_s^{(k-1)} - 2\rho\rho^{(k)} \sum_{i=1}^{N_e} (\mathbf{t}_i - \mathbf{t}_i \odot \mathbf{m}_{c;i}^{(k-1)}) \quad (25)$$

$$\mathbf{m}_{c;i}^{(k)} = \mathbf{m}_{c;i}^{(k-1)} - 2\rho\rho^{(k)} \mathbf{t}_i \odot (A_c - \mathbf{m}_s^{(k-1)}) \quad (26)$$

$$\mathbf{m}_s^{(k)} = F^{(k)}(\mathbf{r}_s^{(k)}). \quad (27)$$

where

$$\mathbf{t}_i = \Phi_i^T [\Phi_i (\mathbf{m}_s^{(k-1)} + (A_c - \mathbf{m}_s^{(k-1)}) \odot \mathbf{m}_{c;i}^{(k-1)}) - \mathbf{d}_i]. \quad (28)$$

All results shown in this paper are obtained with the first model but we describe the second one here for future reference.

## 4. Training

### 4.1. Training dataset

The neural network is trained with simulated light curves of exoplanets in many different configurations. The main ingredients that we need to simulate are the  $\Phi$  matrices, which only depend on the geometry of the problem, and the surface  $\mathbf{m}_s$  and cloud albedos  $\mathbf{m}_c$ , which changes from planet to planet. The training

set is then formed by the triplet  $(\mathbf{m}, \mathbf{d}, \Phi)$  for each example in the training database for cloudless planets. Likewise, for cloudy planets we have the quadruple  $(\mathbf{m}_s, \mathbf{m}_c, \mathbf{d}, \Phi)$  considering all observed epochs in which the cloud coverage changes.

For the definition of the planetary surface and cloud albedos we use the Hierarchical Equal Area and isoLatitude Pixelization (HEALPix<sup>2</sup>). HEALPix has some desirable properties (equal area pixels, efficient available software,...) and has become a standard for the pixelization of the sphere, especially in astrophysics (e.g., Planck Collaboration et al. 2020). For this work we fix  $N_{\text{side}} = 16$ , which results into 3072 pixels on the surface of the planet.

Geometric kernels are used by our neural approach consistently following the ISTA iterative scheme so that they do not need to be learned by the neural network. Therefore, we can get very good generalizations to arbitrary geometries by only simulating a sufficient amount of possible geometries and observing epochs in the training set. More crucial is the process for the generation of the surface albedos. This is precisely the information that is exploited by the neural network to *denoise* each step of the iterative scheme and project the solution on the set of compatible solutions.

We simulate 5000 different  $\Phi$  matrices by randomly setting the rotational period from 10 to 50 days, the orbital period from 100 to 500 days, and the obliquity and inclination of the orbit from 0 to  $\pi/2$ . The parameters  $\phi_{\text{rot}} = \phi_{\text{orb}} = \pi$  are kept fixed given their arbitrary character. Although one should consider

<sup>2</sup> <http://healpix.sourceforge.net>

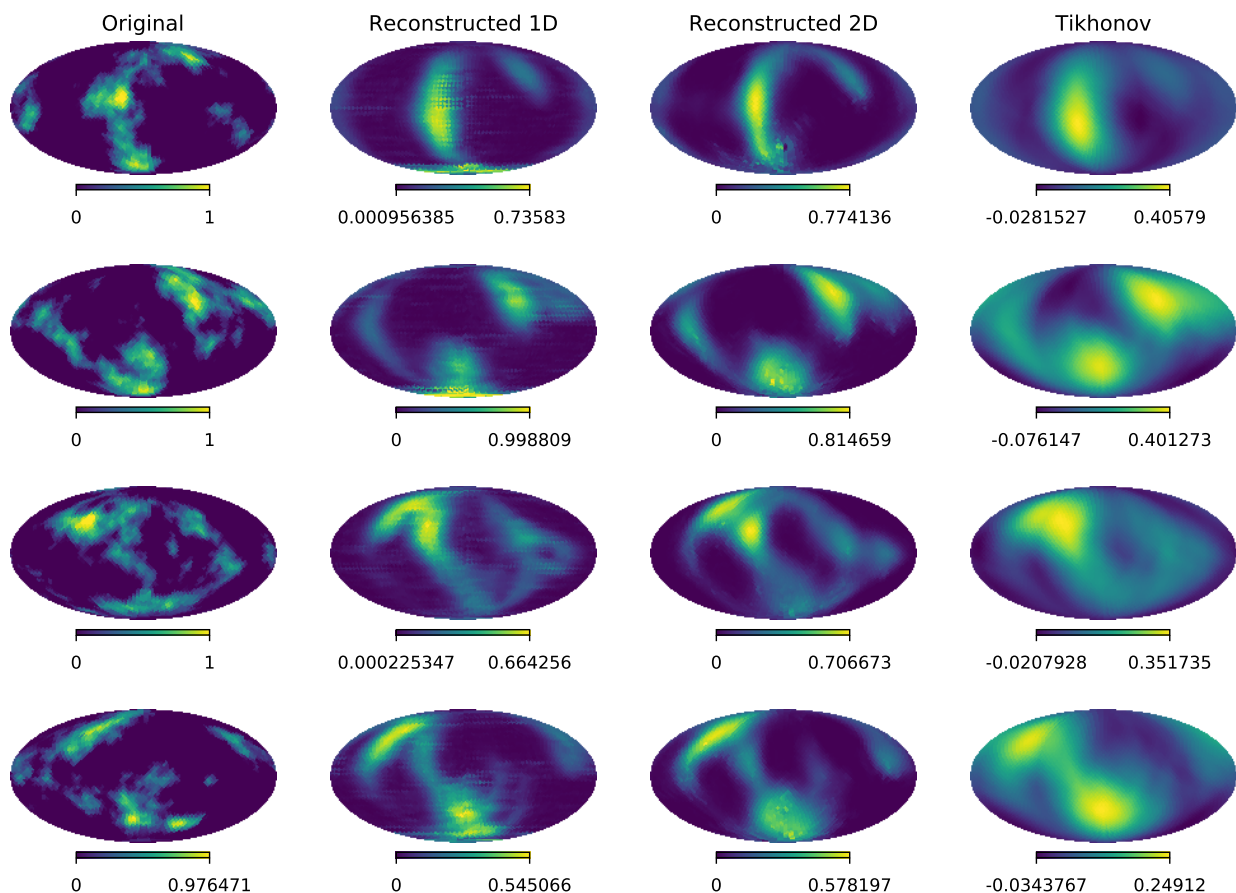


**Fig. 4.** Neural and Tikhonov reconstructions of four different mock cloudless planets observed at the same 5 epochs as those of the training set. In this case, all of them share  $P_{\text{rot}}=24$  h,  $P_{\text{orb}}=365$  days,  $\theta_{\text{orb}}=0^\circ$  and  $\zeta=90^\circ$ . We show the reconstructions carried out with 1D and 2D convolutional networks.

varying them in suitable ranges to cover a good variety of potential  $\Phi$  matrices, we think that this covers a good amount of potential planet candidates observations. For a full description of the  $\Phi$  matrix requires the definition of the specific observing times of each epoch. We assume we observe the planet in 5 epochs that are fixed as multiples of the rotation period, in particular (30, 60, 150, 210, 250). Each epoch consists of observations in steps of 1 hour during an observing period of 24 hours. During this 24 hours interval, global clouds maps are fixed to their daily mean. All  $\Phi$  matrices are computed with the *exocartographer* software package (Farr et al. 2018), using the HEALPix pixelization.

The generation of mock exoplanet surfaces is crucial for the success of the algorithm. The neural network will produce overly simple albedo surfaces if one feeds it with simple surfaces. Therefore, we need to generate sufficiently complex mock albedo surfaces that can look like potential exo-Earths. One option is to use the Gaussian process generation from Farr et al. (2018). However, inspired by the computer graphics procedural generation of planetary surfaces, we prefer to use 3D Perlin noise (Perlin 1985). We use the open source *libnoise* library<sup>3</sup> that generates correlated noise in the surface of the sphere to produce a database of mock procedurally-generated planetary surface and cloud albedos. Three examples of the generated surface and cloud albedos are shown in Fig. 3, together with the final albedo computed with Eq. (17). We generate 5000 pairs of mock

albedo surfaces and clouds for the training by modifying the seed of the Perlin noise generator. The surface albedo contains large zones of low albedo which can be compatible with oceans.

#### 4.2. Training the neural network

The training proceeds by chunking the training set in batches of size  $N_b = 128$  cases for the denoiser that uses one-dimensional convolutions and  $N_b = 32$  for the denoiser that uses two-dimensional convolutions in the sphere (the reduction in the batch size comes from limitations in the GPU memory). These batches are then fed to the unrolled neural network in sequence. For each batch, our aim is to force the discrepancy between the reconstructed albedo map and that of the training set to be as small as possible. The loss function to be minimized is:

$$\mathcal{L} = \sum_{i=1}^{N_b} \sum_{k=1}^N \omega_k \|\mathbf{m}_i^{(k)} - \mathbf{m}_i\|_2^2. \quad (29)$$

Note that we force all phases of the unrolled neural network to produce intermediate solutions that get close to the albedo map in the training set (with weight  $\omega_k$ , that we set to  $\omega_k = 1$ ), instead of just the final output,  $\mathbf{m}^{(N)}$ . We found that this produced a slightly faster behavior during training. The learnable parameter set includes the weights of all the convolutional layers of  $F$  as well as the step sizes  $\rho^{(k)}$ . We additionally force  $\rho^{(k)}$  to be in the interval  $[0.1, 3]$ .

<sup>3</sup> <http://libnoise.sourceforge.net/index.html>

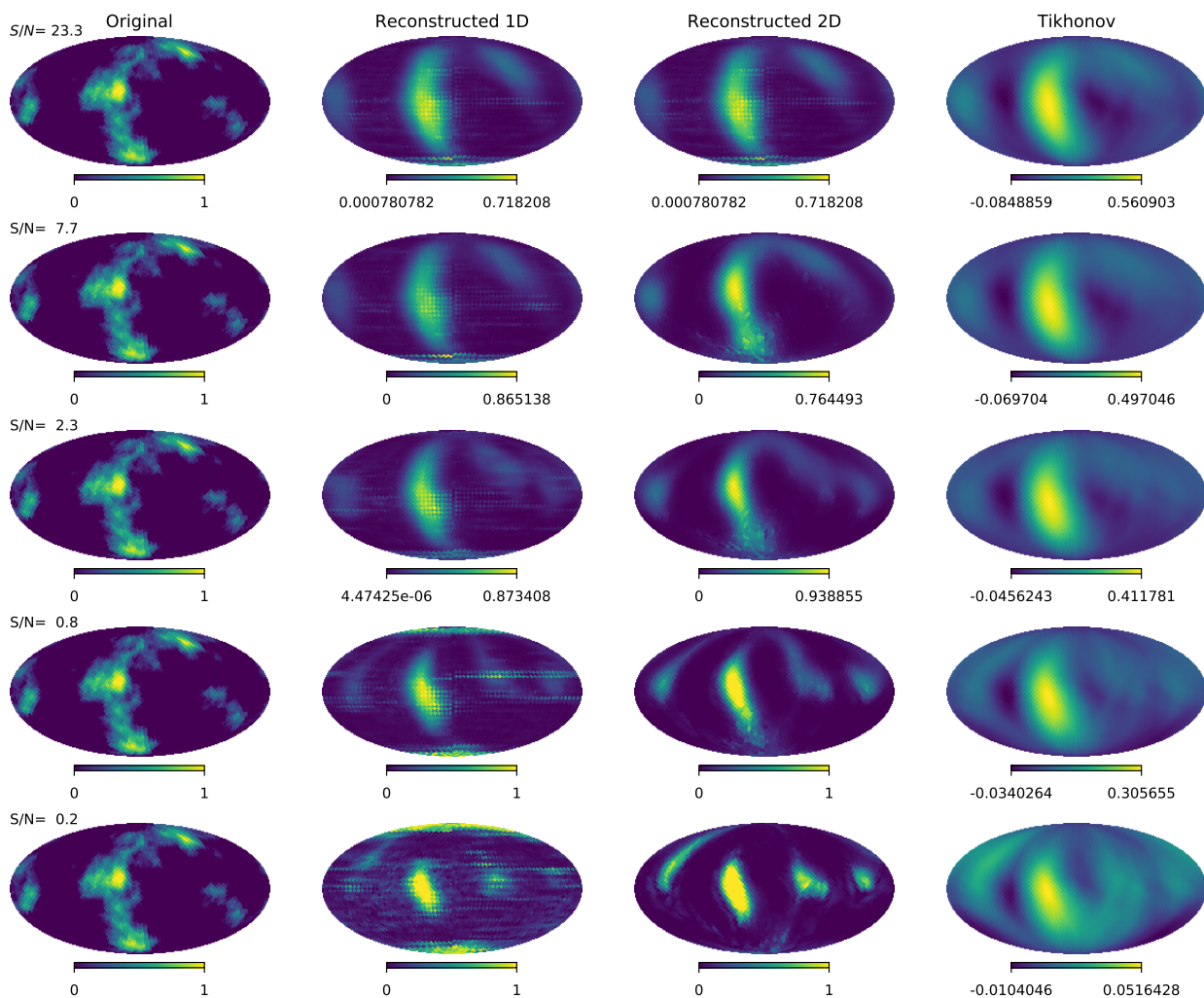


**Fig. 5.** Noise sensitivity of the reconstruction of a mock planet. The geometric parameters are the same as those in Fig. 4 and the signal-to-noise ratio of the light curve is shown in each case.

We define and train the unrolled deep neural network in PyTorch 1.6 (Paszke et al. 2019), which can efficiently compute the gradient of the loss with respect to the parameters using automatic differentiation. We use the Adam stochastic gradient optimizer (Kingma & Ba 2014), with a learning rate of  $3 \times 10^{-4}$  during 50 epochs. We found that the chosen learning rate produces suitable results and it was kept fixed for all experiments. During training,  $N_b$  geometrical kernels and albedo surfaces are randomly picked up from the available database to construct each batch. A total of 20k simulated light curves are used in each epoch of the training. We utilize an NVIDIA RTX 2080 Ti GPU for the computations and the computing time per epoch during training is  $\sim 60$  s in the case of 1D convolutions and  $\sim 11$  min in the case of 2D convolutions. A set of unseen validation examples is also reconstructed with the network at the end of each epoch to check for overfitting. At the end of training we freeze the neural network parameters that produces the smallest loss function in the validation set for producing the results shown in the next section.

## 5. Results

### 5.1. Cloudless mock planets

We start by analyzing the results when new mock albedo surfaces are used using the two options that we consider for the denoising operators, i.e., using 1D or 2D convolutions in the sphere. Although having fast reconstructions is not a real issue at the moment we point out that the reconstruction of a map with 3072 pixels can be done in  $\sim 6$  ms when using 1D convolutions and in  $\sim 11$  ms when 2D convolutions are used. These reconstruction times are obtained by making use of the GPU and do not take into account any memory transfer time between the main memory and that of the GPU or viceversa, which is often times a limiting factor. The quoted times include the application of the  $N = 15$  unrolled steps, together with the application of the denoising neural networks in each step. Although we impose the loss function over all steps of the unrolled iterative scheme, the results we show are those obtained in the last step.

The reconstruction of four mock planets are displayed in Fig. 4. The parameters are  $P_{\text{rot}} = 24$  h,  $P_{\text{orb}} = 365$  days,  $\theta_{\text{orb}} = 0^\circ$  and  $\zeta = 90^\circ$ . This corresponds to a face-on observation of the star-planet system, with the planet spinning axis contained in the ecliptic plane. This configuration, although probably not dynamically stable, allows us to see the planet continuously spinning,

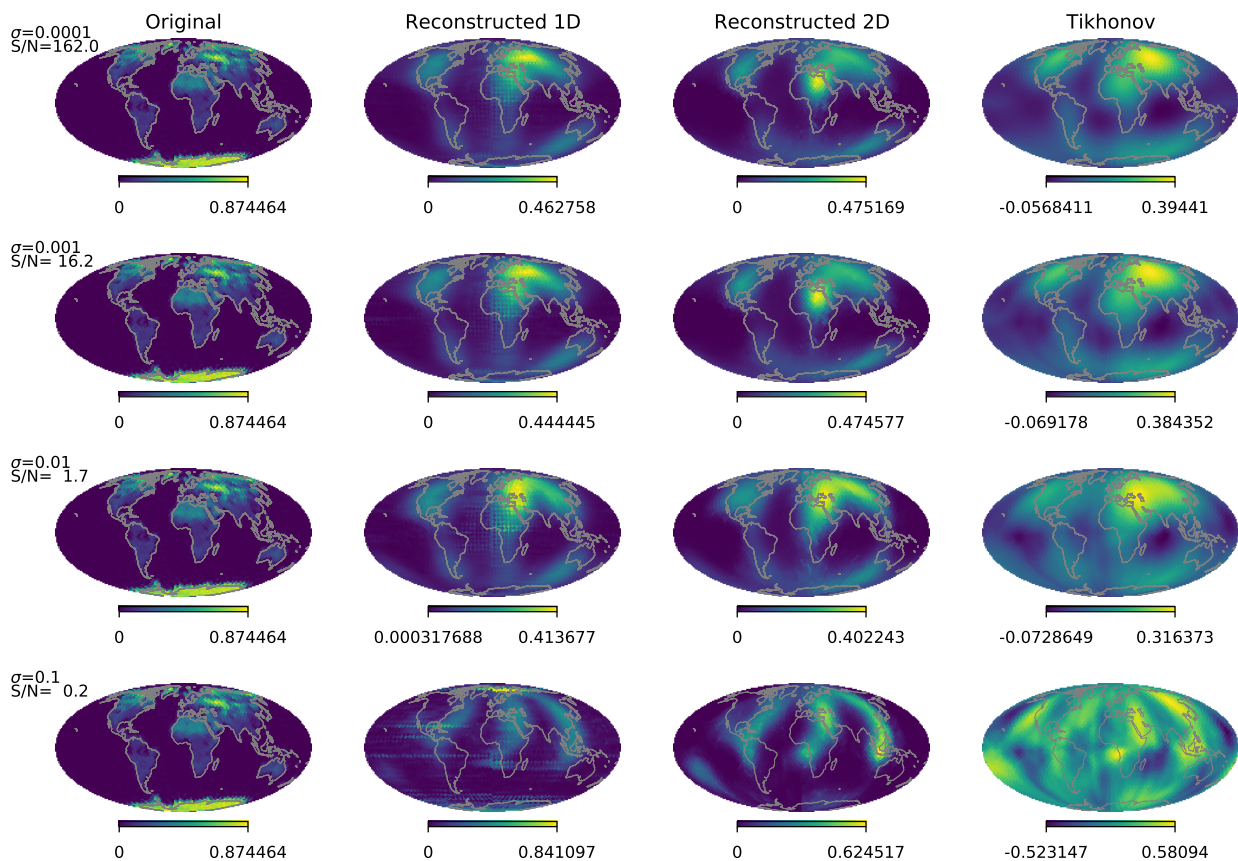


**Fig. 6.** Reconstruction of the cloudless Earth at different  $S/N$ . The parameter  $\sigma$  refers to the standard deviation of the noise added to the light curve. The coastlines are shown for reference.

while the illuminated hemisphere changes during the orbital period. We also chose this configuration for easy comparison with previous works that often made use of it (e.g., Kawahara & Fujii 2011; Kawahara & Masuda 2020). The planet is observed at the same 5 epochs used during training, which turns out to be a very sparse sampling of the light curve. The noise injected on the light curve is such that we end up with a  $S/N = 2.3$ . The left column shows the original map, the middle columns show the two neural reconstructed albedo maps, while the last column displays the map inferred with the Tikhonov regularization with  $\lambda = 0.5$  and using the optimal value of  $\rho$ . The value of  $\lambda$  was found by trial-and-error looking for the most contrasted reconstruction without visible artifacts. Both neural reconstructions show a quite remarkable resemblance with the original map except for some of the high spatial frequency variations. We note that the artifacts in the 1D regularizer come from the fact of not imposing any spatial coherence during the regularization. One of the most conspicuous artifacts is a checkerboard-like structure that disappears when using the 2D regularizer. All our experiments suggest that the 2D regularizer should be taken as the baseline.

The neural reconstruction produces much more compact large albedo regions, in closer agreement with the original maps. However, both reconstructions are unable to reach the amplitude of the largest albedo regions. Likewise, the very low or zero albedo regions in the original map are reconstructed with slightly larger albedos, which are used to compensate for the large albedo regions. It is clear that the neural reconstruction leads to a much better representation of the albedo map than the Tikhonov-regularized one. Interestingly, we find no visible

artifacts on the reconstruction in the poles, even though the observational configuration has no access to them.

The neural reconstruction is very resilient to the presence of noise in the light curve, as shown in Fig. 5 for a single mock surface. The geometric parameters are kept fixed and equal to those of Fig. 4. Increasingly larger amounts of noise are injected in the observed light curve, giving rise to a broad variation in the  $S/N$  ratio, from 0.2 to 23. The value of the regularization parameter in the Tikhonov reconstructions has been optimized, by trial-and-error, to produce the best result possible. It is obvious that the Tikhonov regularization struggles to reconstruct the low albedo regions when the noise is very large, while the neural approach consistently recovers a very robust map, even for very small  $S/N$ . When the  $S/N$  is very low, both the neural and Tikhonov reconstructions display regions with large albedos that were not present in the original surface.

## 5.2. Cloudless Earth

As an example of the reconstruction of a cloudless planet we show the reconstruction of the Earth albedo. The albedo map that we use corresponds to February 2017, obtained from the NASA Earth Observation (NEO) webpage<sup>4</sup>. We simulate the observation of the Earth for  $\theta_{\text{orb}} = 0^\circ$  and  $\zeta = 90^\circ$ . The light curve is observed for one orbital period (365.25 days) with a cadence of 5 hours, producing a total of  $\sim 1750$  points in the light curve. We assume that the observations are instantaneous, neglecting the smearing effect produced by the rotation. Both

<sup>4</sup> See <https://neo.sci.gsfc.nasa.gov>.

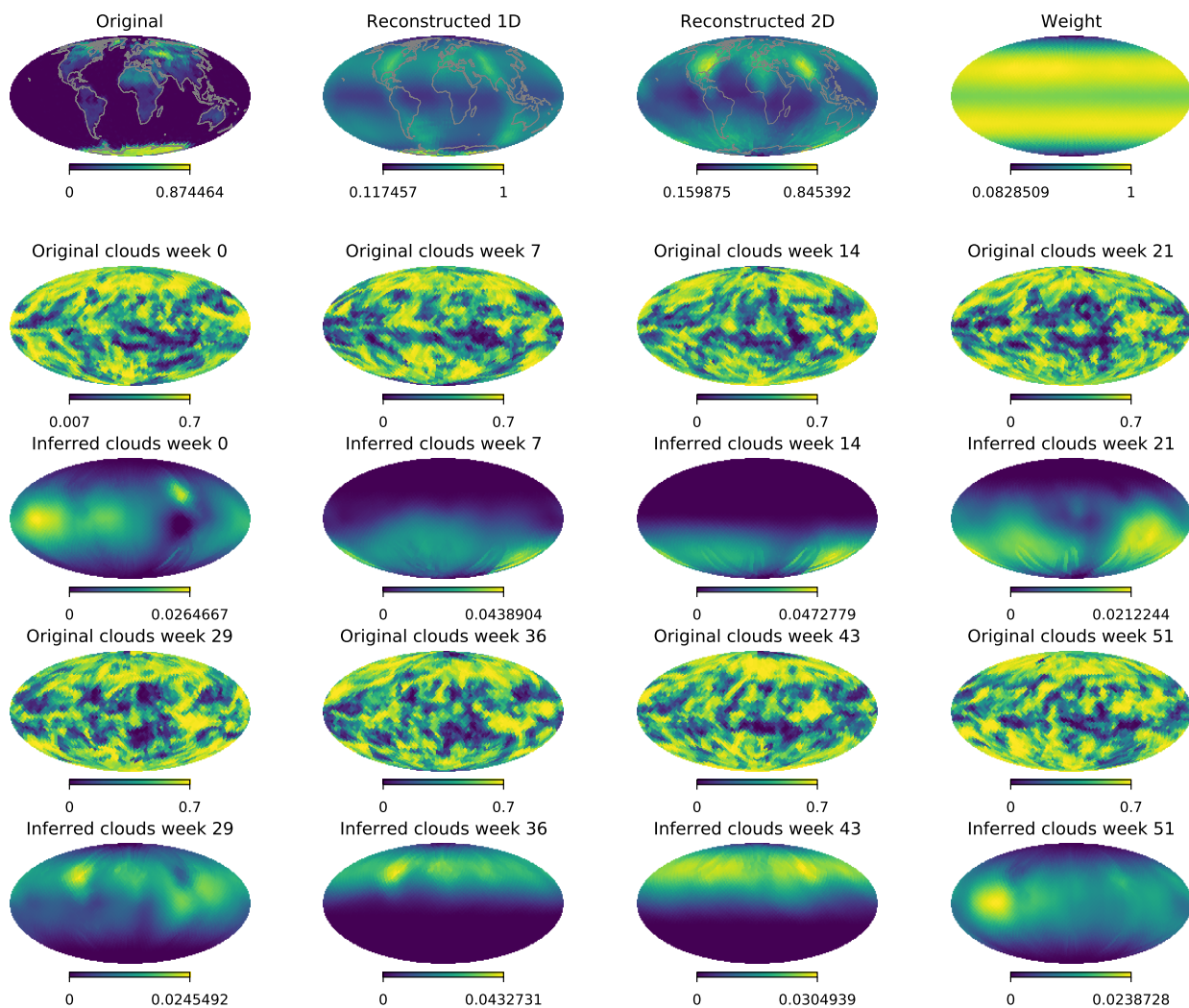


**Fig. 7.** Reconstruction of a cloudy exo-Earth when observed face-on, with  $\theta_{\text{orb}} = 0^\circ$  and  $\zeta = 90^\circ$ . The upper row shows the original surface albedo map, together with the two reconstructions using different denoisers, as well as the relative weight for each element in the surface. The next pairs of rows display the original cloud coverage (rows 2 and 4), together with the inferred cloud albedo (rows 3 and 5).

neural reconstructions displayed in Fig. 6 produce very reliable maps of the surface albedo of the Earth. Almost all continents (North America, South America, Europe, Asia and Africa) are clearly recovered, with their fine structure in the albedo. The large albedo of the Sahara desert, central Asia and the northern part of North America are very well recovered even when the  $S/N \sim 1$ , with almost the same extension as in the original surface albedo. Antarctica is not recovered properly because of the limited access to the poles in this configuration. Additionally, Australia is recovered at a different latitude.

On the contrary, the Tikhonov regularized maps show very smooth continents. The reconstruction is very robust to the presence of noise on the light curve. Even when the signal is buried in the noise, with a very low  $S/N = 0.2$ , the reconstruction is very robust. Some details are lost and in some cases artifacts appear. However, a comparison with what be achieved with Tikhonov shows the potential for the learned regularization.

### 5.3. Cloudy Earth

We now turn our attention to the difficult problem of mapping cloudy planets. We analyze whether the surface of an exo-Earth

and the clouds can be mapped with our neural approach. To this end, we assume that we observe the Earth during a year with a cadence of 5 hours with a  $S/N = 16$ . We use the same surface albedo that was used for the cloudless Earth mapping of Fig. 6. The Earth’s daily-averaged cloud cover maps are obtained from the daily 20-year database of the International Satellite Cloud Climatology Project<sup>5</sup> (Rossow & Bates 2019). We arbitrarily chose to use the data from year 2004. Even though the database contains a different cloud cover map each day, we make the simplifying assumption that the cloud covering is stable for one week. Since the typical lifetime of large-scale cloud pattern on earth is about 1-week (Pallé et al. 2008), this makes the problem slightly better constrained.

We consider two observational geometries, both of them allowing a potentially complete mapping of the surface. The first one is a face-on observation ( $\theta_{\text{orb}} = 0^\circ$ ) with obliquity  $\zeta = 90^\circ$ . This configuration, similar to that used in the previous examples, produces an illuminated hemisphere that changes smoothly with the orbit from the north pole to the south pole and viceversa, while the spinning modulation gives information about the structures in the illuminated hemisphere. The second case is an edge-

<sup>5</sup> See <https://isccp.giss.nasa.gov/>

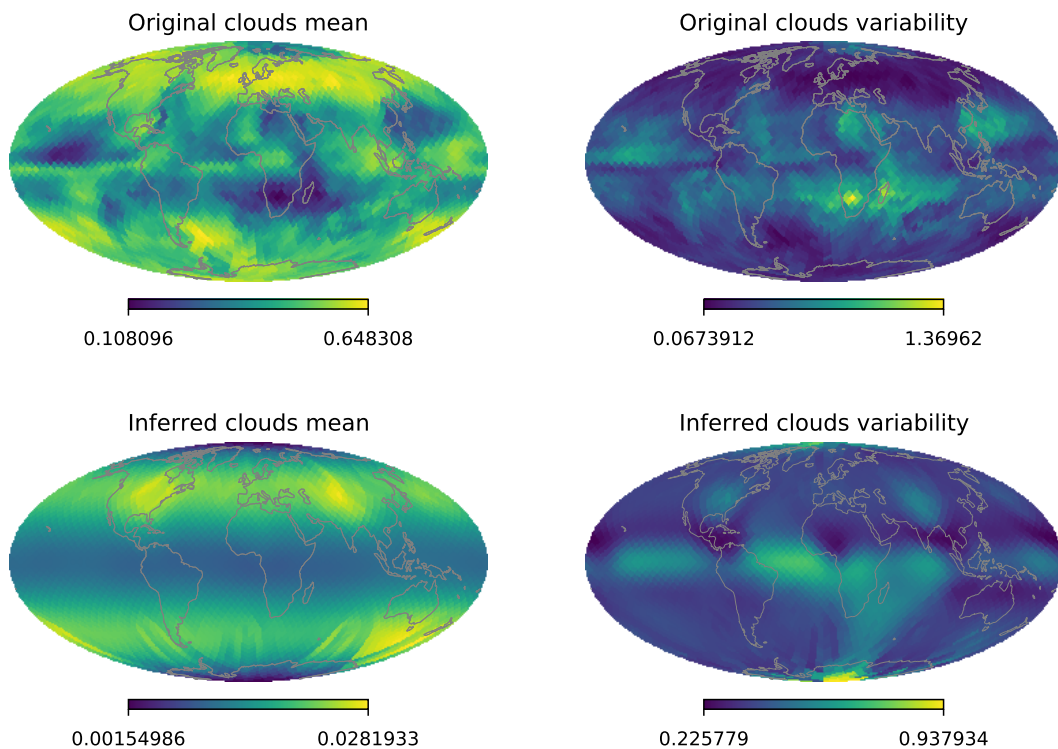


**Fig. 8.** 2004 Yearly-mean cloud cover on Earth (top left) and an maps of its variability (top right). In the bottom panels are the same recovered maps for a simulated Earth, when observed face-on, with  $\theta_{\text{orb}} = 0^\circ$  and  $\zeta = 90^\circ$ .

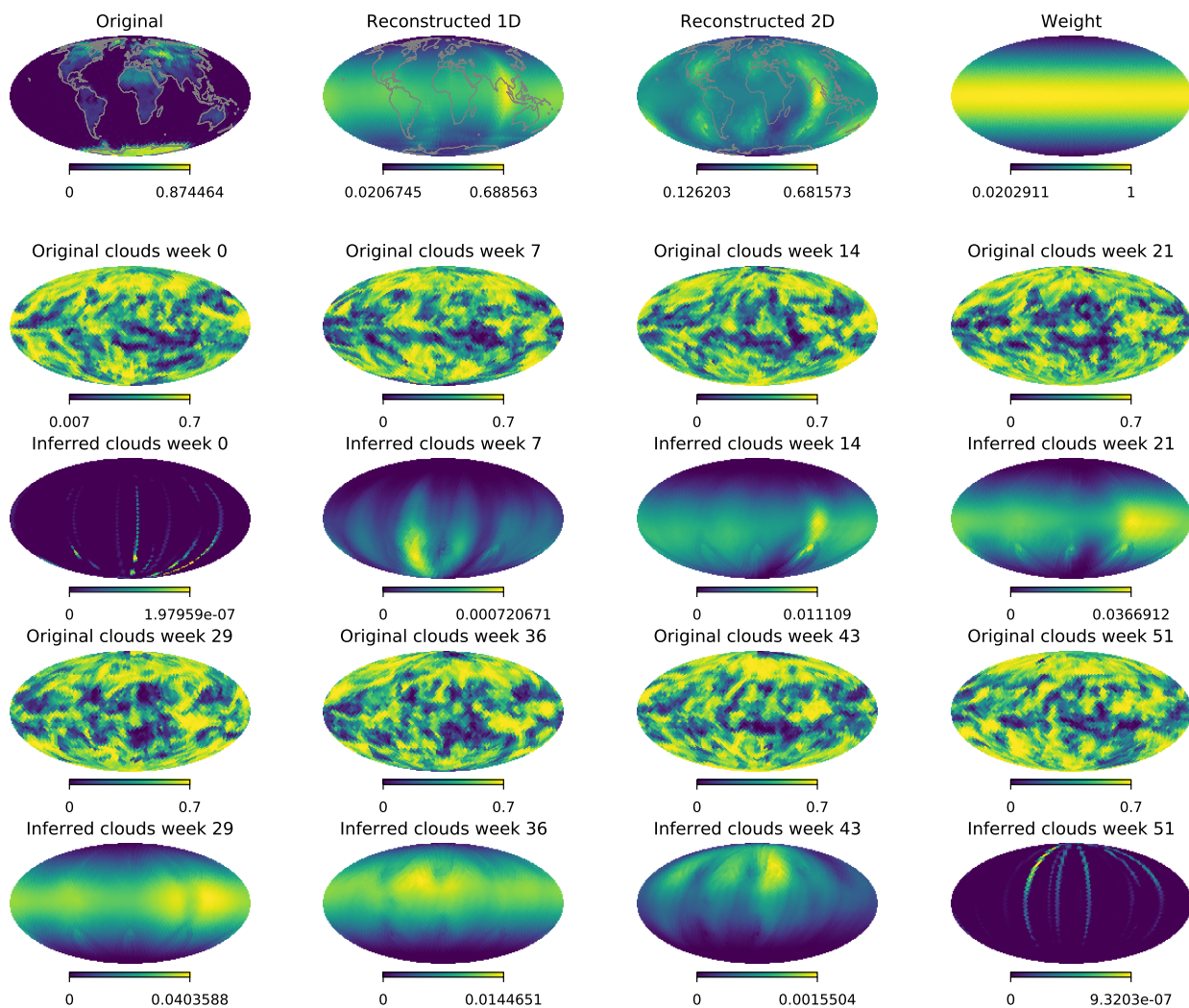
on configuration ( $\theta_{\text{orb}} = 90^\circ$ ) with obliquity  $\zeta = 23^\circ$  without considering the eclipse. This configuration is less informative because the observations are much more sensitive to the equatorial and tropical regions than to those of larger latitude, but it is a much more likely scenarios for real exoplanet observations.

Figure 7 shows the results of applying the neural reconstruction using the two denoisers. The upper row displays the original map, the two reconstructed maps, as well as the weight that this configuration puts on every point on the surface. The remaining rows display the original cloud albedo (rows 1 and 3) and the inferred cloud albedo (rows 2 and 4) for 8 epochs along the year of observation (labeled with the specific week). When compared with Fig. 6, the inferred surface albedos are strongly affected by the presence of the clouds. The large albedo of North America is correctly recovered, but the Sahara desert and the Central Asia high albedo regions are slightly displaced in latitude, probably as a consequence of the persistent clouds, as explained in the following. We have checked that this displacement is reduced and the maps converge towards those of Fig. 6 when the amount of clouds is decreased.

The cloud albedo on each epoch clearly shows the partial information produced by the change in the illuminated hemisphere. We note that the amplitude of the inferred albedo of the clouds is systematically very low. This is probably a consequence of the weak dependence of the total albedo on the specific albedo of the clouds when the surface albedo is large. For this reason, although the learned scheme tends to produce small albe-

dos for the clouds, one can scale them up while still fitting the observations. As a consequence, obtaining absolute cloud albedos seems to be not possible with monochromatic observations.

Even if we cannot obtain the cloud map per epoch, it is worth analyzing if one can recover the mean cloud coverage and, more interestingly, a measure of its variability. The upper row of Fig. 8 shows the 2004 yearly-mean cloud coverage for Earth and its relative variability (defined as the standard deviation normalized by the mean). The most conspicuous features are persistent clouds close to the east coast of South America, in the northern part of America, Europe and Asia and in the southern coast of Australia. These are in good agreement with some of the regions of large albedo obtained in the neural reconstructions. Therefore, we conclude that these reconstructions are able to obtain a combination of the surface albedo, together with the persistent clouds. Additionally, the recovered cloud relative variability (lower row) nicely correlates with the one measured on Earth. Large cloud relative variabilities are found close to the Equator, in southern Africa and in part of eastern Asia. These are areas with strong daily and seasonal cloud variability. Consequently, we conclude that this mapping method is able to obtain a roughly estimate of cloud variability on an exo-Earth. When applied to rocky planets in the habitable zone of their host stars, the bulk atmospheric composition from spectroscopic studies as well as the measured equilibrium temperature of the planet will be able to constrain and associate this cloud variability to that of the water



**Fig. 9.** Like Fig. 7 but for edge-on observation with  $\theta_{\text{orb}} = 90^\circ$  and  $\zeta = 23^\circ$ .

cycle, implying not only water vapor in the planetary atmosphere but also significant amounts of liquid water in the surface.

Finally, we show in Fig. 9 the reconstructions in the edge-on observation. Unfortunately, the limited latitude sensitivity of this configuration introduces an ambiguity in latitude of all structures that cannot be overcome. Still the recovered “D-shaped” maps capture well the three major continental features of the original maps (Americas, Europe/Africa and Asia) and thus the inhomogeneity of the planetary surface. We have been unable to significantly improve the quality of the mapping by increasing the duration of the light curve. As a consequence of the poor mapping of the surface, the cloud mapping is also defective and the cloud variability is also poorly inferred.

## 6. Conclusions

We have presented a mapping technique for exo-Earths using neural networks as regularizers<sup>6</sup>. The standard iterative scheme for the solution of linear problems with regularization is unrolled as a neural network and trained in an end-to-end fashion. The best regularizer is found to be a convolutional neural network acting on the surface of the planet. Given the absence of observed maps of exo-Earths, we use albedo surfaces generated

procedurally trying to mimick our planet. The mapping technique is general and can be re-trained in case better options for albedo surfaces are found in the future.

We apply the method to cloudless planets, showing that the surface of such planets can be very well recovered with our methodology. The position of the continents and their extension shows a clear improvement with respect to more standard regularizations like Tikhonov. Additionally, the results are extremely resilient to the presence of noise on the light curve. We also show how cloudy planets can also be roughly mapped with the same method using only monochromatic observations. The inferred albedo maps contain information about a combination of the surface albedo and persistent clouds, which cannot be disentangled. This degeneracy can potentially be broken if polychromatic observations are used if clouds and surface albedos have a different behavior with wavelength (Cowan et al. 2009).

Finally, although detailed cloud mapping for each observing epoch cannot be accurately retrieved, we show that we can obtain a good estimation of the mean persistent cloud distribution and, more importantly, their map of variability. If applied to rocky planets in the habitable zone of their stars, this cloud variability maps, together with the measured bulk atmospheric composition and equilibrium temperature of the planet, will be able to constrain the presence of a water cycle in the planetary

<sup>6</sup> [https://github.com/aasensio/neural\\_exocartography](https://github.com/aasensio/neural_exocartography)

atmosphere/surface. Thus, our method implies the potential to empirically infer the presence of significant amounts of liquid water in the planet's surface.

*Acknowledgements.* We acknowledge financial support from the Spanish Ministerio de Ciencia, Innovación y Universidades through project PGC2018-102108-B-I00 and FEDER funds. This research has made use of NASA's Astrophysics Data System Bibliographic Services. We acknowledge the community effort devoted to the development of the following open-source packages that were used in this work: `numpy` ([numpy.org](http://numpy.org), [Harris et al. 2020](https://doi.org/10.1007/978-1-4939-9734-4)), `matplotlib` ([matplotlib.org](http://matplotlib.org), [Hunter 2007](https://doi.org/10.1007/978-1-4939-9734-4)), `PyTorch` ([pytorch.org](http://pytorch.org), [Paszke et al. 2019](https://doi.org/10.1007/978-1-4939-9734-4)) and `zarr` ([github.com/zarr-developers/zarr-python](https://github.com/zarr-developers/zarr-python)).

## References

- Aizawa, M., Kawahara, H., & Fan, S. 2020, *ApJ*, 896, 22
- Beck, A. & Teboulle, M. 2009, *SIAM J. Imaging Sciences*, 2, 183
- Berdugina, S. V. & Kuhn, J. R. 2019, *AJ*, 158, 246
- Candès, E. J., Romberg, J. K., & Tao, T. 2006, *Communications on Pure and Applied Mathematics*, 59, 1207
- Cowan, N. B., Agol, E., Meadows, V. S., et al. 2009, *ApJ*, 700, 915
- Des Marais, D. J., Harwit, M. O., Jucks, K. W., et al. 2002, *Astrobiology*, 2, 153
- Farr, B., Farr, W. M., Cowan, N. B., Haggard, H. M., & Robinson, T. 2018, *AJ*, 156, 146
- Ford, E. B., Seager, S., & Turner, E. L. 2001, *Nature*, 412, 885
- Fujii, Y. & Kawahara, H. 2012, *ApJ*, 755, 101
- Goodfellow, I., Bengio, Y., & Courville, A. 2016, *Deep Learning* (MIT Press), <http://www.deeplearningbook.org>
- Gregor, K. & LeCun, Y. 2010, in *Proc. International Conference on Machine Learning (ICML'10)*
- Hardegree-Ullman, K. K., Cushing, M. C., Muirhead, P. S., & Christiansen, J. L. 2019, *AJ*, 158, 75
- Harris, C. R., Millman, K. J., van der Walt, S. J., et al. 2020, *Nature*, 585, 357–362
- Hunter, J. D. 2007, *Computing in Science Engineering*, 9, 90
- Kawahara, H. 2020, *ApJ*, 894, 58
- Kawahara, H. & Fujii, Y. 2010, *ApJ*, 720, 1333
- Kawahara, H. & Fujii, Y. 2011, *ApJ*, 739, L62
- Kawahara, H. & Masuda, K. 2020, *ApJ*, 900, 48
- Kingma, D. P. & Ba, J. 2014, *CoRR*, abs/1412.6980
- Krachmalnicoff, N. & Tomasi, M. 2019, *A&A*, 628, A129
- Léger, A., Mariotti, J. M., Mennesson, B., et al. 1996, *Icarus*, 123, 249
- Luger, R., Agol, E., Foreman-Mackey, D., et al. 2019a, *AJ*, 157, 64
- Luger, R. & Barnes, R. 2015, *Astrobiology*, 15, 119
- Luger, R., Bedell, M., Vanderspek, R., & Burke, C. J. 2019b, *arXiv e-prints*, arXiv:1903.12182
- Meadows, V. S., Reinhard, C. T., Arney, G. N., et al. 2018, *Astrobiology*, 18, 630
- Pallé, E., Ford, E. B., Seager, S., Montañés-Rodríguez, P., & Vazquez, M. 2008, *ApJ*, 676, 1319
- Pallé, E., Zapatero Osorio, M. R., Barrena, R., Montañés-Rodríguez, P., & Martín, E. L. 2009, *Nature*, 459, 814
- Pallé, E., Zapatero Osorio, M. R., & García Muñoz, A. 2011, *ApJ*, 728, 19
- Parikh, N. & Boyd, S. 2013, *Proximal Algorithms*, *Foundations and Trends in Optimization* (Now Publishers)
- Paszke, A., Gross, S., Massa, F., et al. 2019, in *Advances in Neural Information Processing Systems 32*, ed. H. Wallach, H. Larochelle, A. Beygelzimer, F. d'Éric, E. Fox, & R. Garnett (Curran Associates, Inc.), 8024–8035
- Perlin, K. 1985, in *Proceedings of the 12th Annual Conference on Computer Graphics and Interactive Techniques, SIGGRAPH '85* (New York, NY, USA: Association for Computing Machinery), 287–296
- Perraudin, N., Defferrard, M., Kacprzak, T., & Sgier, R. 2019, *Astronomy and Computing*, 27, 130
- Planck Collaboration, Aghanim, N., Akrami, Y., et al. 2020, *A&A*, 641, A1
- Rossow, W. B. & Bates, J. J. 2019, *Bulletin of the American Meteorological Society*, 100, 2423
- Snellen, I. A. G., de Kok, R. J., le Poole, R., Brogi, M., & Birkby, J. 2013, *ApJ*, 764, 182
- Tarter, J. C., Backus, P. R., Mancinelli, R. L., et al. 2007, *Astrobiology*, 7, 30
- Venkatakrishnan, S. V., Bouman, C. A., & Wohlberg, B. 2013, in *2013 IEEE Global Conference on Signal and Information Processing*, 945–948
- Wang, L., Sun, C., Fu, Y., Kim, M. H., & Huang, H. 2019, in *2019 IEEE/CVF Conference on Computer Vision and Pattern Recognition (CVPR)*, 8024–8033
- Zhang, J. & Ghanem, B. 2018, in *Proceedings of the IEEE conference on computer vision and pattern recognition*, 1828–1837